10TH INTERNATIONAL SYMPOSIUM ON PARTICLE IMAGE VELOCIMETRY - PIV13
Delft, The Netherlands, July 1-3, 2013

Characterization by PIV of the Effect of Vortex Generators in a Transonic Separated Flow

F. Sartor, G. Losfeld, B. Leclaire, R. Bur

ONERA, 8 rue des Vertugadins, 92190 Meudon, France.
fulvio.sartor@onera.fr

ABSTRACT

The present study is aimed to analyse the effect of passive vortex generators in a transonic interaction between a shock-wave and a turbulent boundary layer in a channel flow at Mach number M = 1.45. Control of the boundary layer detachment downstream of the shock is obtained thanks to momentum transfer given by passive control devices, mechanical vortex generators (VG), located upstream of the shock and distributed in the spanwise direction. The channel's lower wall is equipped with a contour profile - a bump - allowing flow separation. Two-component PIV velocity measurements are performed using the iterative gradient-based cross-correlation algorithm FOLKI-SPIV developed at ONERA. The evolution of the bulk flow and of the separated bubble due to the shock-wave boundary layer interaction is accurately quantified. Changes in the turbulent behaviour are also analysed thanks to the fluctuating fields. Comparisons with the already known flow without control give an appraisal of the effectiveness of such devices.

1. Introduction

Shock wave/boundary layer interaction has been the subject of several studies during the last 60 years [11], as it is encountered in a variety of applications, both in the case of external and internal flows. The interaction, which is one of the simplest occurrences of a strong inviscid-viscous interaction, often leads to separation, source of high amplitude fluctuations related to the development of large turbulent structures in the recirculation. As a result, significant undesirable effects are obtained on the performance of rocket or aircraft, such as drag rise, fall of aerodynamic efficiency and wall heating [10]. Flow control aiming at preventing as much as possible this separation is thus a problem of foremost importance, and has motivated a large body of work in past studies.

Among the various possible strategies, mechanical vortex generators (VG), whose effect is well known in simpler, subsonic flows, have received a large attention. Indeed, they often manage to offer a flexible and low cost solution to prevent separation: thanks to an induced vorticity, they increase the mixing between the higher momentum external flow and the low momentum near-wall flow, energizing the boundary layer that becomes less prone to separate [32, 28]. Aside from this direct objective, which may result in aircraft wing lift, other uses of these devices can also be to tailor wing-buffet characteristic at transonic speed [9], and to reduce fluctuating pressure loads for buffet control [2]. A disadvantage in using VG is however the introduction of a parasitic drag component, which can be countered while maintaining the same efficiency by choosing low-profile vortex generators (sub-VG) [28]. Past studies also compared the respective performance of different shapes of VG, and observed that the optimal shape is the vane type [27]. These VG consist of a row of small plates or airfoils normal to the surface and set at an angle of incidence to the local flow, in order to produce an array of streamwise trailing vortices.

According to Hadjadj et al. [22], the SWBLI problems can be divided into three families: the transonic shock-boundary layer separation, the oblique shock impinging turbulent boundary layer and supersonic flow over a compression ramp. To the authors knowledge, among these three different SWBLI configuration, research has focused mainly on compression ramp [17], corner flow [36] and impinging shock wave interaction [12, 24, 38]. Recently, the supersonic flow with incident shock wave has been preferred for PIV studies, both in uncontrolled configuration [25] and with control devices [4]. However, few PIV studies [23, 35] have been applied to a transonic interaction with a strong shock wave that causes massive separation of the boundary layer. Even considering LDV investigation [8, 30], a deeper physical understanding is still needed for this particular case that presents the additional disadvantage that, in the same field, a supersonic, a high subsonic and a low speed reverse flow zones coexist. From a technical point of view, due to the presence of a high turbulence level resulting from the boundary layer separation, further seeding problems arise in addition to the classical complication of the supersonic flow PIV.

The present study's objective is to take a step forward in the physical analysis of the effect of mechanical VG on SWBLI in the transonic regime. We focus on one type of VG, which has been shown by [5] to lead to a significant decrease in the separation. This device is of the conventional type, i.e. not a sub-VG. As a matter of fact, it leads to larger vortices, whose effect is thus easier to measure. We perform in particular two-component PIV measurements and use the same experimental settings and methods as in [35], in which the reference case without control has been carefully documented. In particular, as in this study, we take advantage of the specificities of the ONERA software FOLKI-SPIV, which allows high-speed and flexible processing [7].

After a description of the set-up and measurements, the article will quantify the effect of the vortex generators. This will be done not only by investigating the evolution of the mean velocity field, but also by considering that of turbulent quantities in the mixing layer zone, where the momentum transfer, responsible for the increase of the vorticity in the boundary layer, indicates where the control device is effective.

2. Experimental set-up

2.1 Flow properties

The experiments were performed in the S8Ch supersonic wind tunnel of the ONERA Meudon centre, a continuous wind tunnel supplied with desiccated atmospheric air. The stagnation conditions were near ambient pressure and temperature: $p_{st} = 0.96 \cdot 10^5 \pm 300$ Pa and $T_{st} = 300 \pm 10K$. The test set-up consists of a transonic channel having a test section of 100 × 120 mm, as shown in figure 1. The upper wall is rectilinear, whereas the lower wall is a contoured profile designed to produce a uniform supersonic flow of nominal Mach number equal to 1.45. A second throat of adjustable cross section allows to produce a shock-wave in the test section by choking effect.

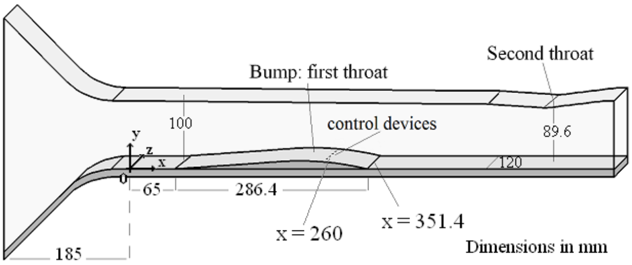

Figure 1: Scheme of the test section.

Figure 2: Photo of S8Ch wind tunnel.

As depicted in figure 1, x, y and z respectively denote streamwise, crosswise and spanwise directions. Corresponding velocity components will be respectively denoted by u, v and w. Two component LDV measurements [5] showed that at $x = 135$ mm the boundary layer on the bump is fully turbulent with the following characteristics: physical thickness $\delta = 4$ mm, displacement thickness $\delta^* = 0.46$ mm and momentum thickness $\Theta = 0.25$ mm. The associated unit Reynolds number is around $Re = 14 \times 10^6$ m^{-1}, which leads to a value of $Re_\Theta = 3500$. The experimental conditions are summarized in table 1. The velocity $U_\infty = 300$ m.s^{-1} is used as a reference to build dimensionless quantities; it corresponds to a typical value of the average velocity in the shear layer.

Parameter	**Value**	**Description**
U_∞	300 m.s^{-1}	Reference velocity
p_{st}	$0.96 \cdot 10^5 \pm 300$ Pa	Total pressure (inlet condition)
T_{st}	300 ± 10 K	Total temperature
M	1.45	Mach number
δ	4 mm	Boundary layer physical thickness
δ^*	0.46 mm	Boundary layer displacement thickness
Θ	0.25 mm	Boundary layer momentum thickness
Re	14×10^6 m^{-1}	Unit Reynolds number
Re_Θ	3500	Momentum Reynolds number

Table 1: Flow and boundary layer properties.

To visualize the flow field and control the shock position in the test section, a Schlieren apparatus is used. As any light source disturbs the PIV camera, the Schlieren visualization is employed only to check the initial condition when the wind tunnel is started. Then, the position of the shock is monitored by the evolution of static pressure through 36 pressure taps located on the lower wall, at mid-span. Previous studies [16] have indeed showed that there is an optimal position of the lambda shock to achieve the maximal size of the recirculation zone, obtained when the tangent of the shock normal to the lower wall is 12.5 mm downstream of the downstream end of the bump. This optimum is the situation considered here. Figure 3 shows a Schlieren visualization of the corresponding flow in the uncontrolled case, which has been accurately quantified in a previous study [35] and will be used as a reference case. A large separation indeed occurs, starting from the shock foot, and whose extent will be further characterized below. Note that in this configuration, the nominal Mach number is approximately 0.75 downstream of the shock.

2.2 Control devices

Among the wide kind of control devices, the most important are shock-control methods such as passive devices using cavity [6, 34], mesoflaps based on recirculation transpiration [20], active control using blowing or suction [9, 26], 3-D bumps [31], which work by generating compression waves that smear the shock-induced pressure rise, and micro-ramps, [4] that generate packets of individual vortex pairs downstream of their vortices. A comparative study [29] between two kinds of passive control showed that vortex generators leads to a viscous drag lower than the passive control using cavity, which justifies the present choice to control the boundary layer separation downstream of our shock-wave.

In practice, VG are located upstream of the shock and distributed in the spanwise direction, as shown in figure 4. Their main objective is to transfer streamwise momentum in the lower layers of the boundary layer in a continuous process, and thus to provide a continuous source of re-energisation to counter the natural boundary layer deceleration and growth caused by surface friction and adverse pressure gradient. Larger adverse pressure gradients or stronger shock waves can thus be imposed without causing separation. The family of

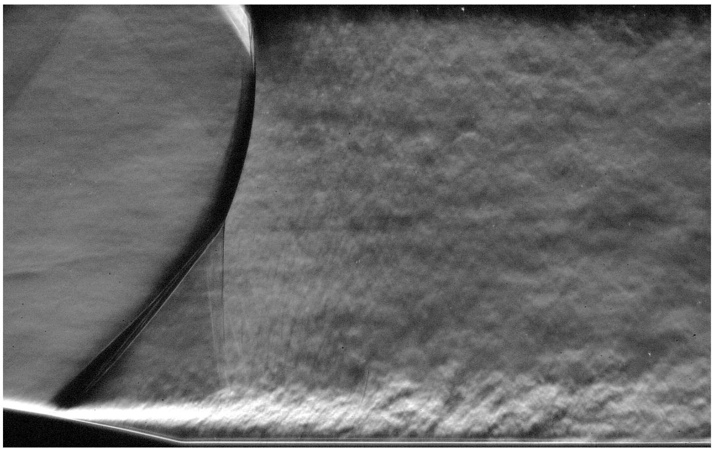

Figure 3: Schlieren visualization of the uncontrolled flow (from [35]).

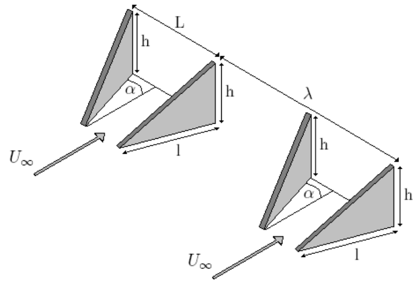

Figure 4: Geometrical characteristics of our triangular vane-type VG.

vane-type vortex generators can be divided into many types, depending on the shape, the orientation of the lifting surface and on the size. According to the findings of by Ashill et al. [1] and Godard and Stanislas [21], triangular vane-type VG constitute an optimal geometry. Relying on the device height h, we can distinguish conventional VG, in which the incoming boundary layer thickness is the same order than the VG device height ($h \approx \delta$), and low-profile VG, or sub-VG, (with $h < \delta/2$). The most important single factor in establishing an effective vortex pattern is the need to keep the spacing of adjacent vortices above a certain minimum value, represented by the parameter λ/h: only if the initial spacing of the vortices is greater than about three times their height is the system efficient [28]. If the space between two pairs of VG is too small compared with the size of a single VG, the vortices will merge too quickly and lose their efficiency.

Parameter	Value	Description
h	4,0 mm	VG device height
l	5,0 mm	VG device length
L	6,0 mm	Distance between two VG
λ	20,0 mm	Distance between a pair of VG
N	5	Number of VG
α	18°	Angle of attack

Table 2: Geometrical parameters of the vane-type VG.

In an LDV study on forced shock oscillations, Bur et al. [5] have compared the effect of several of these VG systems in the present configuration. We here consider one of the most efficient of these, i.e. symmetric VG that induce counter-rotating vortices, and whose geometrical characteristics are gathered in table 2. Each VG plate is a triangular element whose leading edge is located at $x = 260$ mm, and whose angular position is fixed at 18° with regard to the main flow direction. The plate height is that of the boundary layer, i.e. $h \approx \delta$. The number of VG has been adapted in order to cover the entire span of the test set-up. The VG plates are located along a line situated 10 mm downstream of the bump crest. This position, as other geometrical parameters, has been selected between what has been proposed by Lin [28] and by the numerical simulations of Lee et al. [27].

2.3 *PIV system*

We use a double pulse Nd:YAG laser, which delivers 150mJ per pulse, operating at 5.6 Hz. Two longitudinal planes are investigated: one is located exactly in the middle of one VG pair and coincides with the test section mid-span, $z = 60$ mm. It is denoted by "on VG" in the figures. The other is located between two different pairs of VG (denoted by "between" in the figures), at $z = 70$ mm. The former plane allows to describe the turbulent wake developing downstream of the vortex generators, while the latter is pivotal to characterize the effectiveness of the vortices spanwise spreading. Note that in the reference case [35], the laser sheet was located at $z = 55$ mm in order to avoid perturbations due to the presence of Kulite sensors at the lower wall. More details on this will be given in section 3.1. In all cases, the laser sheet thickness was comprised between 1 and 1.5 mm. Figure 5 illustrates graphically the respective position of the laser sheet with respect to the devices and the generated vortices. The laser pulse separation is 2.5 μs, which is adapted to the large velocities considered here.

The camera is equipped with a 105 mm focal length; as the CCD sensor is 2048 × 2048 pixels, the resulting magnification ratio is around 20 px/mm. . The access for the laser light is provided by a window on the top wall of the wind tunnel, so that the light direction is towards decreasing y.

To achieve the most regular seeding it was convenient to locate the particle generator far upstream of the test chamber, so that the tracers have time to mix with the flow and create a uniform cloud of particles. Liquid particles of Di-Ethyl-Hexyl-Sebacat (DEHS)[1], were used as tracer. The DEHS oil has a density of about $\rho_p = 900 kg/m^3$ and the generator provides a nominal particle size of $d_p = 0.5\mu$m. In [35], the actual average particle diameter and corresponding response time τ_p have been determined thanks to a profile of Mach number

---

[1] Produced by an atomizer aerosol generator Topas Gmbh ATM 210.

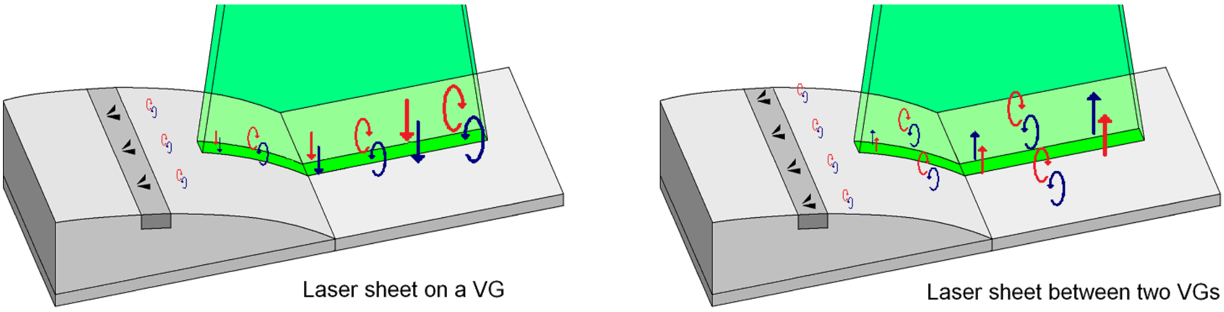

Figure 5: Sketch of the bump with the control device and the induced vortices, together with the different laser sheet positions.

around the shock wave. It was found that the diameter is slightly higher in practice, leading to a resulting Stokes number is of about 0.09, which guarantees the passive nature of the tracer.

The images are processed with the ONERA in-house software FOLKI-SPIV [7], already used in [35], which is implemented on GPU and relies on a Lucas-Kanade paradigm (iterative gradient-based correlation maximization). In the present study, an interrogation window of 17 × 17 pixels has been used; this size corresponds to a physical length of 0.85 mm in the object plane. Further details on how the PIV processing has been adapted to the present configuration can be found in [35].

At each run, 1000 samples are acquired, in order to build average quantities. Note that in the following, upper case variables will denote the mean velocity components, and fluctuations will be denoted by primed lower-case variables (e.g., U and u' for the horizontal component). An assessment was performed to verify the statistical convergence of these average quantities for the present number of samples. For every variable, we consider a residual field, defined as the difference between the average field calculated with 1000 images pairs, and that calculated with a number of images equal to n. If we call $v_i(n)$ the average field of variable number i calculated with n images pairs, the corresponding residual $R_i(n)$ is given, at each field point, by the absolute value of the difference between $v_i(1000)$ and $v_i(n)$. For each n, we then build a global residual by performing a surface integral of the residuals fields for each variable, and we normalize this quantity with a reference value. The right side of figure 6 shows the evolution of this quantity, $Residual_i(n)$, as a function of the image number n. It confirms that 1000 images lead to a satisfactory convergence of both mean and fluctuating velocity components.

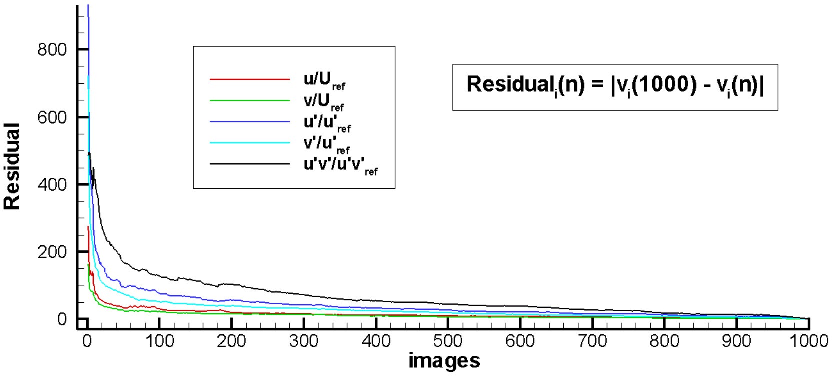

Figure 6: Statistical assessment to verify the convergence of the main field.

3. Results

3.1 Mean flow

As mentioned above, the principal effects targeted when using vortex generator are a downwards transfer of high streamwise momentum into the lower part of the boundary layer, as well as an increase in the turbulent fluctuations. Both effects are known to have a recognized efficiency in boundary layer control. As depicted in figure 5, due to the organization into successive counter-rotating pairs in the span, the expected added vertical velocity due to the vortices should consist of an alternance of positive and negative contributions. The former should be observed between downstream of two consecutive VG pairs ("between" position), and the latter, in the middle of a VG pair ("on" position).

Upstream of the shock, this effect is clearly visible in the flow. This is illustrated in figure 7, which presents vertical profiles of U, V, u'/U_∞, v'/U_∞ and $-u'v'/U_\infty^2$ at $x = 320$ mm. The vertical transfer is clearly visible on the profile of U: whereas it is clearly inflexional in the reference case (down to the lowest value of y accessible with the present PIV measurements), at the "on" position one observes only a very slight decrease from the bulk velocity close to the wall in the controlled case. Fluctuating quantities also begin their increase for much lower values of y in the latter situation, this being a combined effect of the downwards transfer, and of a more stable mean velocity profile. In the "between" plane on the other hand, the boundary layer appears thicker than in the reference case, with a lower minimal velocity close to the wall. Regarding the fluctuating quantities, the effect seems more complex: indeed, the maximal values,

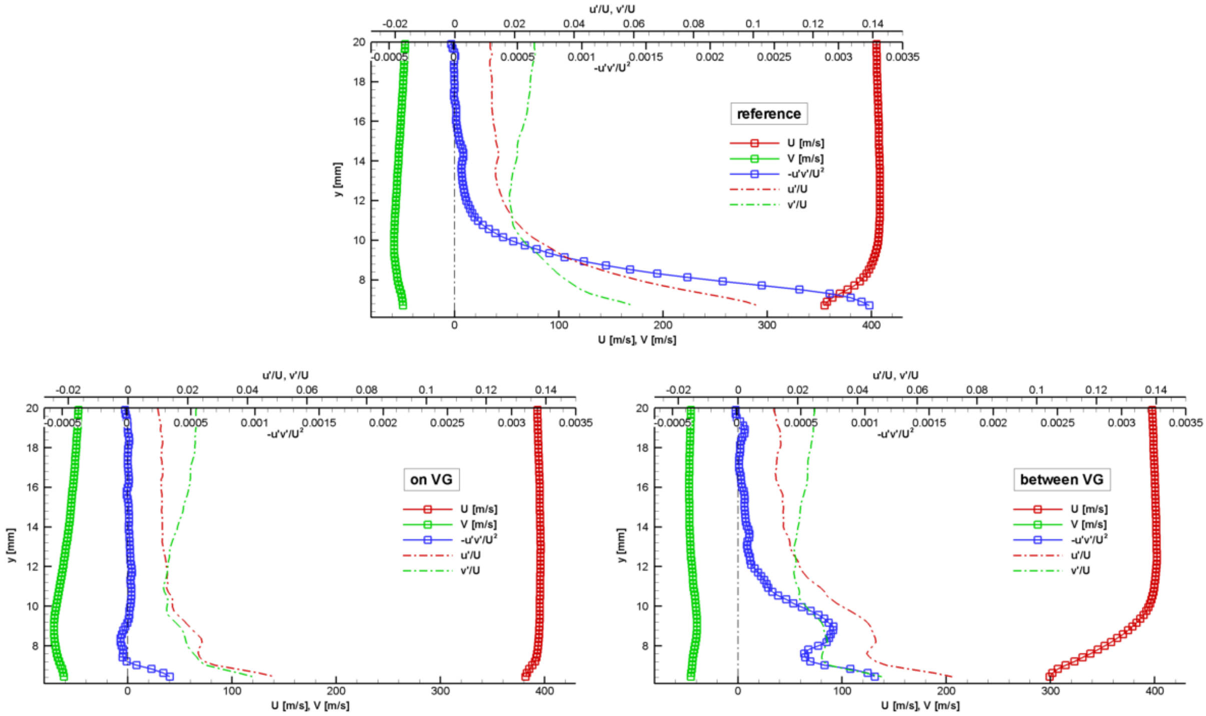

Figure 7: Vertical profiles of U, V, u'/U_∞, v'/U_∞ and $-u'v'/U_\infty^2$ at $x = 320$ mm. Reference case (top), controlled case, "on" (left) and "between" positions (right). Note the different scales used for u'/U_∞, v'/U_∞ on one hand, and $-u'v'/U_\infty^2$ on the other hand.

reached close to the wall, are less important than in the reference case, which might be due to a transfer by the vortices to the third component w'. However, for increasing y starting from the wall one first observes an decrease, then a slight increase to a maximum, followed by a final decrease. Values reached in this local maximum (i.e. close to $y = 9$ mm) are more important than in the reference case, confirming the upwards redistribution of fluctuations.

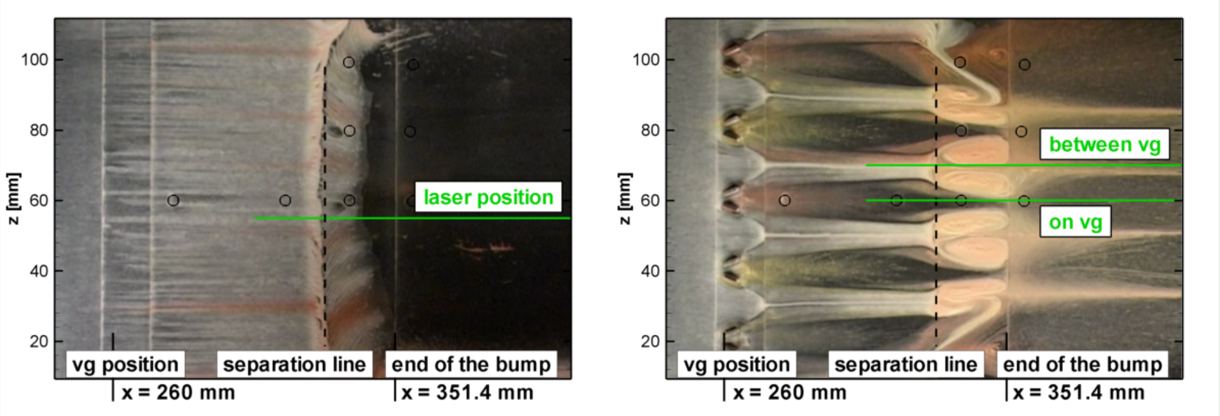

Figure 8: Oil flow visualizations, reference case (left) and controlled case (right). The dashed vertical line identifies the streamwise location of the separation corresponding to the reference case *in both figures*. Black hollow circles highlight small irregularities at the lower wall, due to the presence of (inactive) Kulite sensors.

We now turn to a global description of the controlled flow field. To apprehend the effect of control on its three-dimensional organization, we first consider oil flow visualizations, shown in figure 8. Note that in these figures, the black circles identify the locations of plugged (thus inactive) Kulite sensors, which induce very small and localized irregularities at the lower wall. As will be seen below, these irregularities will however be important enough for the PIV seeding oil to concentrate and form drops, thereby leading to spurious displacements in these zones. This will be evidenced in particular from $x = 335$ mm to $x = 340$ mm in the "on VG" plane. In the reference case, as evidenced by [35], the flow is nearly invariant along the span, and a clear separation, depicted by a black dashed line, is observed. For comparison purposes, this line is traced at its corresponding position in the controlled flow. In this flow, upstream from this line, the skin friction lines mirror the formation and trajectory of the vortices. One observes that once created, each vortex is deflected progressively in the direction of its origin blade's trailing edge, so that pairs of vortices are formed not by both vortices of a VG pair, but by two vortices of adjacent VG pairs. Down to the level of the dashed line, these vortices remain in the form of pairs, as one observes a line of zero friction at their centre. Downstream of the dashed line, one observes a three-dimensional, seemingly

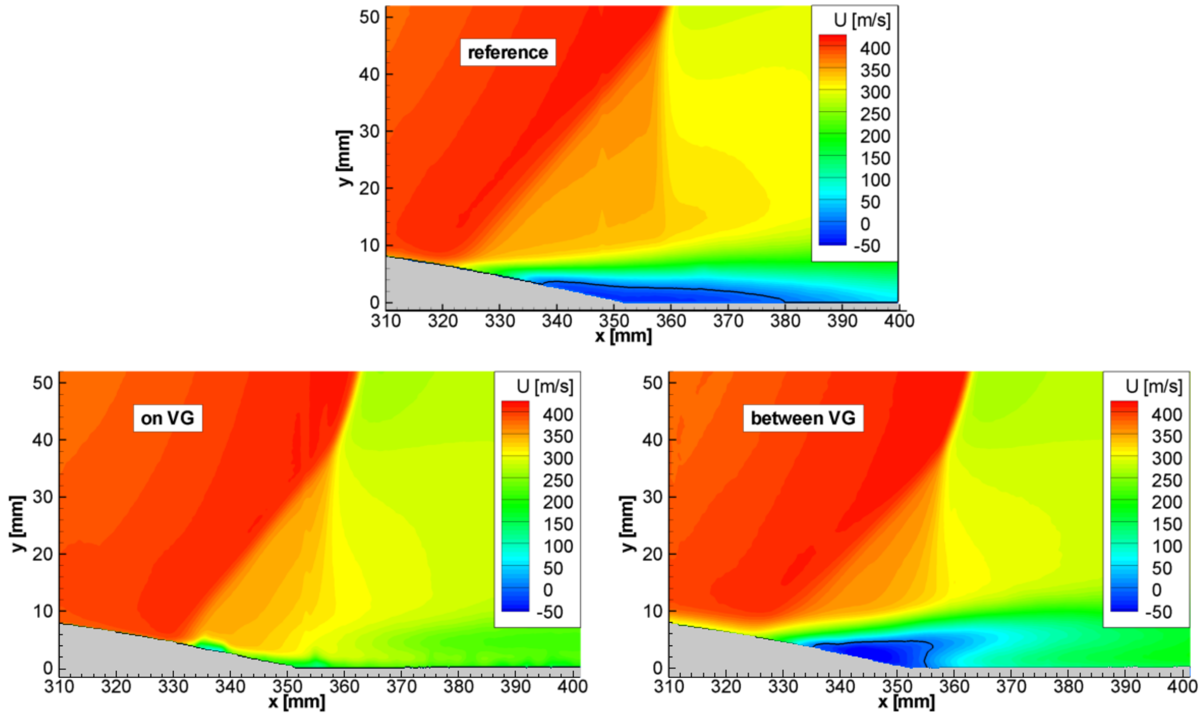

Figure 9: Mean horizontal velocity fields without (top) and with (bottom) vg. The black line identifies the $U = 0$ iso-contour.

spanwise periodic organization of the friction lines. We speak of a seemingly periodicity because we can observe here only two "wavelengths" due to the limited number of VG in the span, and due to the effect of the lateral walls. VG are indeed effective in that there is no separation directly downstream of a VG pair. However, separation cells are observed between two consecutive pairs. Such a situation could be expected, given the qualitative action (induced vertical velocity) of the VG described above. Note that this structure is comparable to that observed by [39], who used delta ramps to control a compression corner flow. Even if the visualization is less precise in that zone, it seems that reattachment occurs close to the downstream end of the bump in the controlled case, i.e. upstream from the reference reattachment. Thus the recirculation cells are smaller than the reference recirculation bubble.

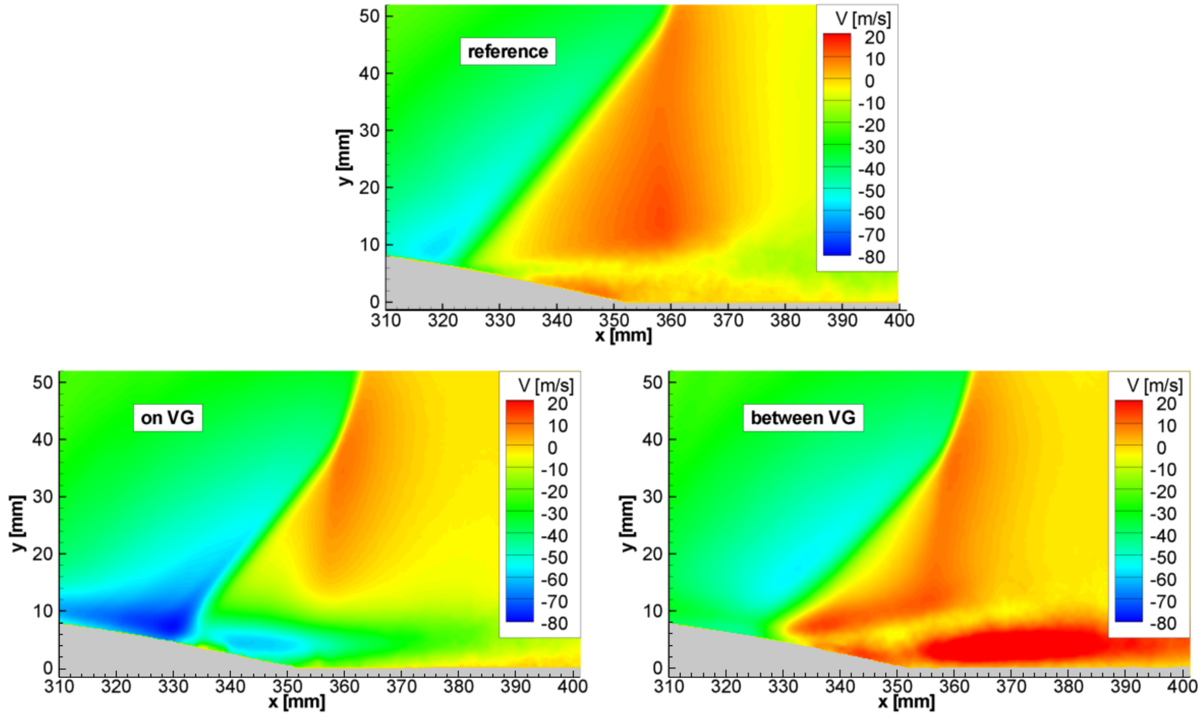

Figure 10: Mean vertical velocity fields without (top) and with (bottom) vortex generators.

These observations are confirmed by the mean velocity fields measured by PIV, whose horizontal and vertical components are plotted in figures 9 and 10 respectively. Focusing first on U, one sees indeed that the recirculation bubble is totally suppressed in the "on" plane, whereas a bubble is present in the "between" plane. While its upstream end is located at the same x as in the reference case, consistent with the skin friction visualizations, its geometry is different: it is of smaller streamwise extent, with a reattachment indeed close to the bump end, but of larger crosswise extent. As will be confirmed by the fluctuation fields, the shear layer in the upper part is lifted upwards compared to the reference case, as a result of the VG induced velocity. Due to this organization, and still contrary to the reference case, vertical profiles of U show the presence of a wake centred roughly around $y = 5$. This will be further described below. Observation of the vertical velocity fields (figure 10) shows that the effect of the VG is detected roughly up to $y = 15$ mm, and that it persists downstream of the shock. As expected, one notes a decrease (resp. increase) in V in the "on" (resp. "between") plane. Note that while we still detect this spanwise alternation of excess and defect in the vertical velocity, which corresponds to the effect of unperturbed vortex pairs, the compression due to the lambda shock probably strongly modifies the topology of the vortices. In particular, complex phenomena such as vortex breakdown could be at play, due to the strong adverse pressure gradient. This hypothesis is consistent with the presence of the axial velocity wake, and should be confirmed by further measurement campaigns, e.g. stereo PIV or tomo-PIV.

3.2 Turbulence

The fields of u'/U_∞ and v'/U_∞ are plotted in figures 11 and 12. As mentioned above, it should be borne in mind that in the "on VG plots", displacements close to the wall between $x = 330$ mm and 335 mm are spurious due to the presence of a Kulite sensor. Looking first at the reference case, one observes that the contribution of the longitudinal velocity is logically the most important (note that the scale is different between u' and v'): the streamwise fluctuations are seen to exceed the vertical fluctuation by a factor of 3. This behaviour indicates the presence of a high anisotropy turbulence in the shear layer above the separation bubble. However, in the most downstream part of the field, where the shear layer ends and v' achieve its maximal values, the energy is nearly equally distributed in the two fluctuations. This occurs through a drop in u', resulting in a decrease in the global turbulent kinetic energy. We can reasonably assume that this decrease is due to a redistribution of the fluctuation from u' to v' and also to the unmeasured w', suggesting a transition towards isotropy.

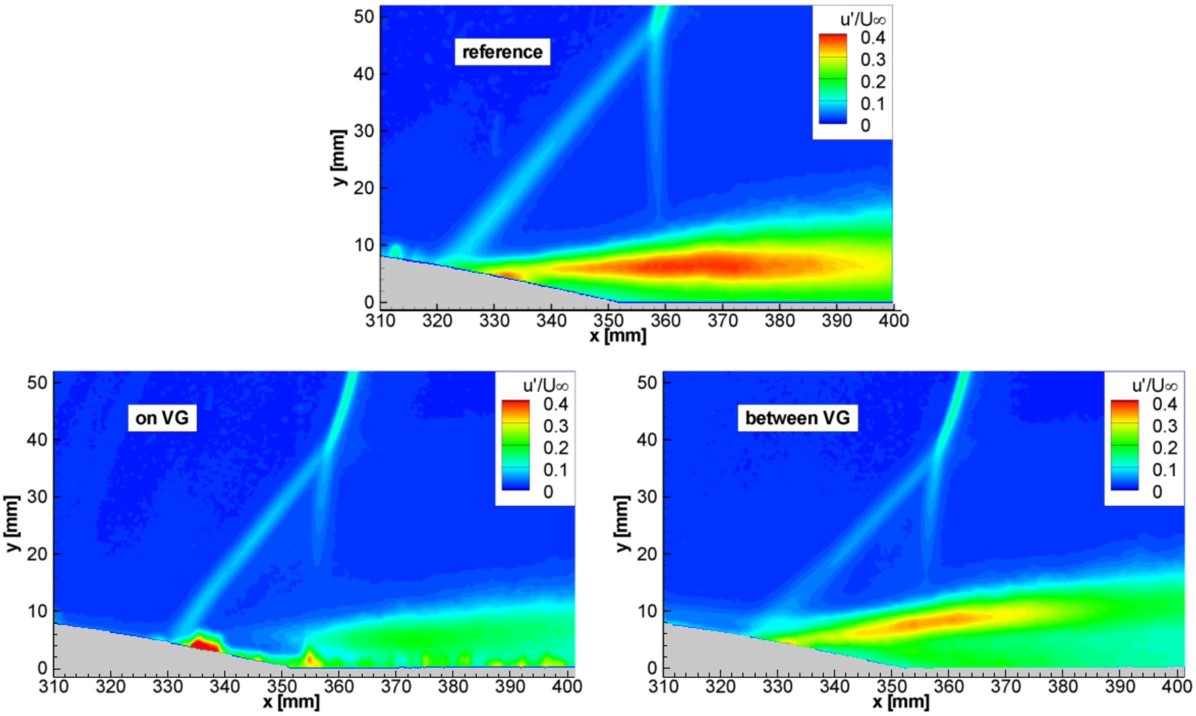

Figure 11: Mean horizontal velocity fluctuation level u'/U_∞ without (top) and with (bottom) vortex generators.

The interpretation of the controlled case is more complex. Indeed, the turbulence observed results both from the specific recirculation structure evidenced in the previous section, as well as the persistence (though probably in a perturbed form) of the vortices created by the VG. Overall, as the flow structure is highly three-dimensional compared to the reference case, one can expect a redistribution of the turbulent motions in all components u', v' and w'. In figure 11, the structural change in u' are coherent with the mean flow dynamics. In the "on VG" plane, where the recirculation is replaced by a thick shear layer downstream of the shock, fluctuations are much less intense than in the reference case. In the "between" plane, a higher but narrower recirculation bubble is observed than in the reference case, and consistently the shear layer is lifted upwards, as shown by the location of the maximum of u'. This maximum is of smaller magnitude than in the reference case. To us, this should be ascribed to a three-dimensional turbulent redistribution. Indeed, it is found (but not shown here for conciseness) that the turbulence production due to the horizontal shear, $P = -u'v' \partial U/\partial y$, is of comparable magnitude in the reference and in the controlled cases, and thus cannot explain the difference in magnitude. Less discrepancies are observed between both cases in the fields of v', except that v' is more important in the "between" plane than in the reference case. This behaviour probably stems from the vortex dynamics; however a more specific mechanism cannot be identified without further

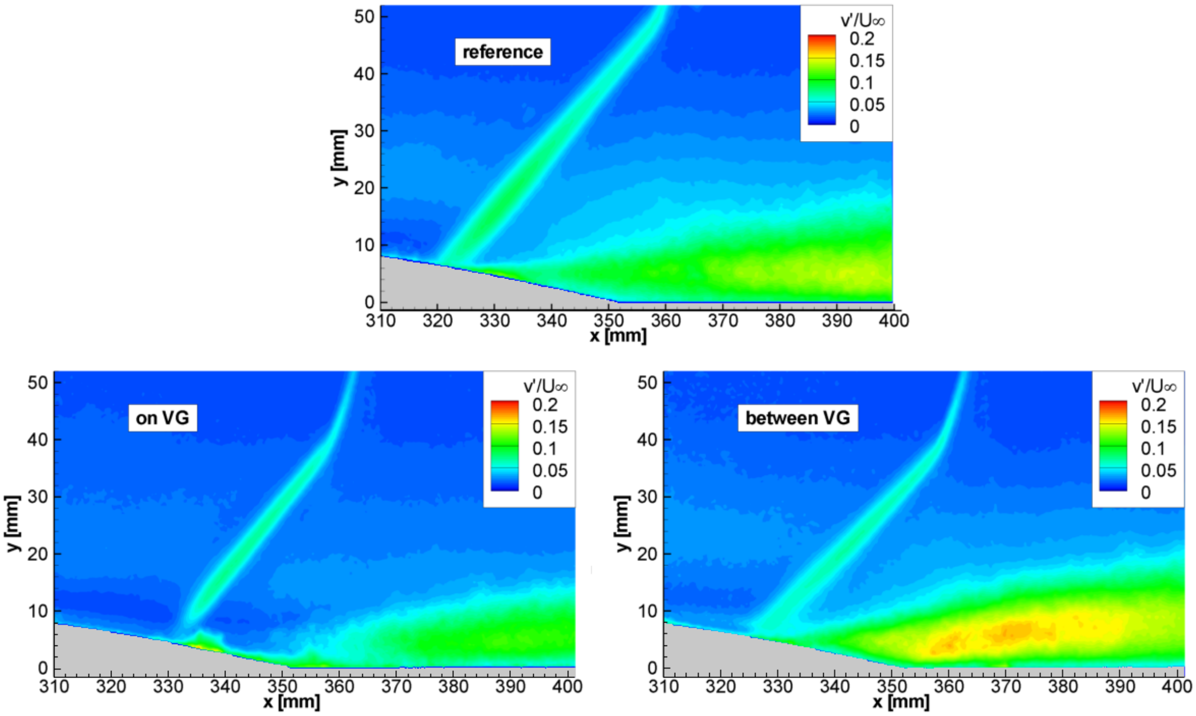

Figure 12: Mean vertical velocity fluctuation level v'/U_∞ without (top) and with (bottom) vortex generators.

measurement data.

Another feature visible in the plots of u' and v' is the signature of the shock wave unsteadiness. This low frequency motion is frequent and has been reported for instance experimentally by [13] or [18] and numerically by [37] or [19]. The frequency is low compared to that involved in the interaction with the boundary layer. Though its origin still remains unknown [14] [15], it can be related to the large scale structure arriving from the upstream boundary layer [3] or be caused by coupling mechanism between the recirculation bubble [33]. In practice, this unsteadiness results here in local fluctuation maxima, which enable to locate the average shock position in a more convenient way than directly from the mean velocity fields.

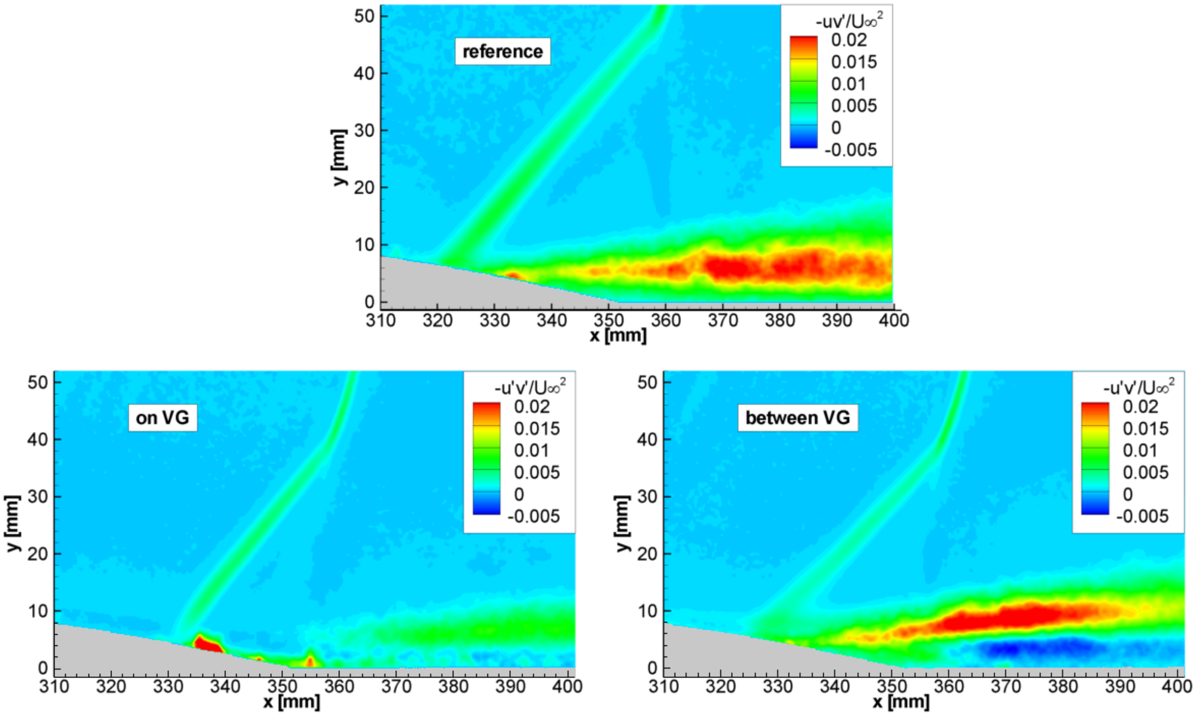

Figure 13: Reynolds shear stress component $-u'v'/U_\infty^2$ without (top) and with (bottom) vortex generators.

As expected from the the transonic nature of the flow, which makes it very sensitive to small perturbations, different shock shapes are observed without and with control. In the controlled configuration the shock maintains its position in the upper part, (around $x = 360$ mm at $y = 50$ mm), whereas there is a shift in the shock leg position. This shift is clear when we observe a field on the VG (the shock foot spreads from $x = 320$ mm to $x = 330$ mm), less remarkable if we observe a field between two VG couples, where the shock foot is around $x = 325$ mm. A similar behaviour can be observed in figure 12.

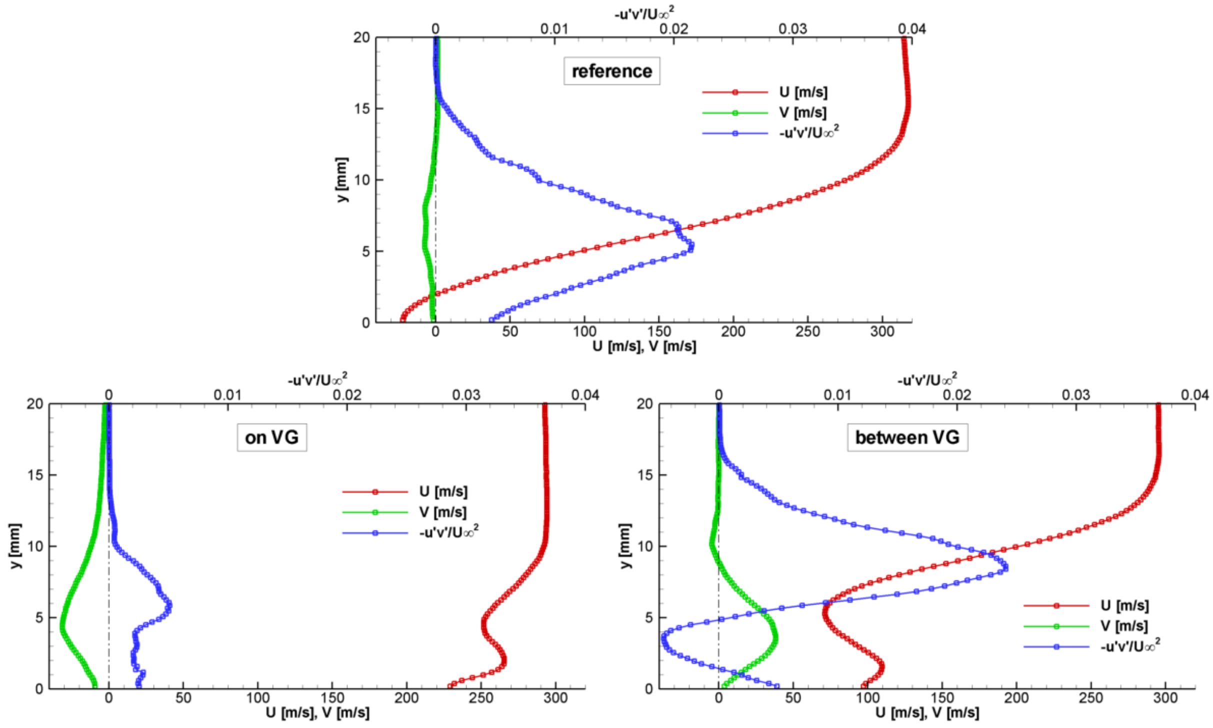

Figure 14: Vertical profiles of U, V and $-u'v'/U_\infty^2$ at $x = 370$ mm, close-up on the near-wall region. Reference case (left) and controlled case (bottom).

Finally, figure 13 shows the distribution of the Reynolds stress component $-u'v'/U_\infty$. If we focus on the field in the wake of a vortex generator we observe, as for u', a decrease of the intensity of the fluctuation compared to the reference field: the main causes are the absence of the recirculation zone and the redistribution of Reynolds stress fluctuations to all the shear stress components, i.e. $u'w'$ and $v'w'$, which are not measured here. Between two VG pairs, the maximum value of $-u'v'$ is comparable to that of the reference case, and coincides with the uplifted position of the shear layer. Below this maximum, one observes a patch of negative values, which is absent in the uncontrolled flow. This patch is directly related to the wake character of the vertical profile of U. This is clearly evidenced in figure 14, where profiles have been extracted at $x = 370$ mm. In particular, one observes that the minimum in $-u'v'$ coincides roughly with the inflexion point of the lower shear layer of the wake. Besides, in an axial sense, this minimum also occurs at the location where the wake in the mean velocity is the most pronounced. This zone of negative $-u'v'$ is indeed absent both in the reference case, and in the "on" plane of the controlled case. In the latter, the mean velocity profile shows only a very slight wake compared to what is observed in the "between" plane.

4. Conclusions

In this study, we have investigated the flow organization resulting from the use of triangular vortex generators in a transonic shock wave/boundary layer interaction on a bump, compared to the reference flow without control. This has been done using skin friction visualizations, and two-component PIV measurements in longitudinal planes located both in the wake of a VG pair, and between two consecutive pairs. Results show that once generated, vortex pairing is formed from vortices of neighbouring VG pairs, and not from the two vortices originating from a single pair. The resulting induced vertical velocity, and its effect on the global flow, are well detected both upstream and downstream of the shock. Control is effective in the sense that the massive separation visible in the reference case is replaced by isolated separation cells, separated by reattached zones. Each of these cells (or bubbles) has a smaller streamwise extent as in the reference case, reattachment occurring roughly at the downstream end of the bump, but a larger crosswise extent. This results in an uplift of the shear layer compared to the reference case, and in the presence of a rather strong wake profile in the mean axial velocity, which in turn induces a symmetric structure of the Reynolds stresses along the crosswise axis. The shock average position is best monitored by the fluctuating quantities, which show that with control, the shock leg position does not change much. It is only slightly shifted downstream, in a larger extent in the wake of a VG pair than between two pairs. Fluctuating quantities globally reflect the mean flow organization in terms of separation and reattachment, with several discrepancies which are hypothesized to originate from the three-dimensional mixing by the vortices. In the plane located in the wake of the vortices, consistent with the reattachment, turbulence remains at weak levels. In the plane cutting a recirculation bubble (between two VG pairs), the uplifted shear layer is less energetic than in the reference case, despite a similar amplitude of the turbulent kinetic energy production term, and larger values of the vertical fluctuation are observed.

Further answers to the observed turbulent behaviour, as well as a more thorough characterization of the flow dynamics, will necessitate measurement tools able to finely characterize the vortices, and their interplay with the compression structure and detachment.

Confirming or infirming hypotheses on their behaviour downstream of the shock, e.g. merging or breakdown, will necessitate more complete diagnosis tools such as tomo-PIV. This challenging objective, which also necessitates advanced algorithms due to the possibility of large optical defects, is the next step we would like to address in future work.

REFERENCES

[1] P.R. Ashill, J.L. Fulker, and K.C. Hackett. Studies of flows induced by sub boundary layer vortex generators (sbvgs). *AIAA Paper*, 968:2002, 2002.

[2] J.W. Barter and D.S. Dolling. Reduction of fluctuating pressure loads in shock/boundary-layer interactions using vortex generators. *AIAA journal*, 33(10):1842–1849, 1995.

[3] S.J. Beresh, N.T. Clemens, and D.S. Dolling. Relationship between upstream turbulent boundary-layer velocity fluctuations and separation shock unsteadiness. *AIAA journal*, 40(12):2412–2422, 2002.

[4] P.L. Blinde, R. Humble, B.W. van Oudheusden, and F. Scarano. Effects of micro-ramps on a shock wave/turbulent boundary layer interaction. *Shock Waves*, 19(6):507–520, 2009.

[5] R. Bur, D. Coponet, and Y. Carpels. Separation control by vortex generator devices in a transonic channel flow. *Shock Waves*, 19(6):521–530, 2009.

[6] R. Bur, B. Corbel, and J. Délery. Study of passive control in a transonic shock wave/boundary-layer interaction. *AIAA journal*, 36(3):394–400, 1998.

[7] F. Champagnat, A. Plyer, G. Le Besnerais, B. Leclaire, S. Davoust, and Y. Le Sant. Fast and accurate PIV computation using highly parallel iterative correlation maximization. *Experiments in fluids*, 50(3):1–14, 2011.

[8] J. Délery. Analysis of the separation due to shock wave-turbulent boundary layer interaction in transonic flow. *La Recherche Aerospatiale*, pages 305–320, 1978.

[9] J. Délery. Flow physics involved in shock wave/boundary layer interaction control. In *IUTAM Symposium on Mechanics of Passive and Active Flow Control: proceedings of the IUTAM Symposium held in Göttingen, Germany, 7-11 September 1998*, volume 53, page 15. Springer Netherlands, 1999.

[10] J. Délery and J.G. Marvin. Shock-wave boundary layer interactions. *AGARDograph*, 1986.

[11] D.S. Dolling. Fifty years of shock-wave/boundary-layer interaction research: what next? *AIAA journal*, 39(8):1517–1531, 2001.

[12] P. Dupont, C. Haddad, and J.F. Debiève. Space and time organization in a shock-induced separated boundary layer. *Journal of Fluid Mechanics*, 559:255–278, 2006.

[13] P. Dupont, S. Piponniau, A. Sidoren, and JF Debiève. Investigation by particle image velocimetry measurements of oblique shock reflection with separation. *AIAA journal*, 46(6):1365–1370, 2008.

[14] J.P. Dussauge, P. Dupont, and J.F. Debiève. Unsteadiness in shock wave boundary layer interactions with separation. *Aerospace Science and Technology*, 10(2):85–91, 2006.

[15] J.P. Dussauge and S. Piponniau. Shock/boundary-layer interactions: Possible sources of unsteadiness. *Journal of Fluids and Structures*, 24(8):1166–1175, 2008.

[16] A. Galli, B. Corbel, and R. Bur. Control of forced shock-wave oscillations and separated boundary layer interaction. *Aerospace science and technology*, 9(8):653–660, 2005.

[17] B. Ganapathisubramani, N.T. Clemens, and D.S. Dolling. Effects of upstream boundary layer on the unsteadiness of shock-induced separation. *Journal of Fluid Mechanics*, 585:369–394, 2007.

[18] B. Ganapathisubramani, NT Clemens, and DS Dolling. Effects of upstream boundary layer on the unsteadiness of shock-induced separation. *Journal of Fluid Mechanics*, 585:369–394, 2007.

[19] E. Garnier, P. Sagaut, and M. Deville. Large eddy simulation of shock/boundary-layer interaction. *AIAA journal*, 40(10):1935–1944, 2002.

[20] D. Gefroh, E. Loth, C. Dutton, and S. McIlwain. Control of an oblique shock/boundary-layer interaction with aeroelastic mesoflaps. *AIAA journal*, 40(12):2456–2466, 2002.

[21] G. Godard and M. Stanislas. Control of a decelerating boundary layer. part 1: Optimization of passive vortex generators. *Aerospace Science and Technology*, 10(3):181–191, 2006.

[22] A. Hadjadj and J.P. Dussauge. Shock wave boundary layer interaction. *Shock Waves*, 19(6):449–452, 2009.

[23] A. Hartmann, M. Klaas, and W. Schröder. Time-resolved stereo PIV measurements of shock–boundary layer interaction on a supercritical airfoil. *Experiments in Fluids*, 50(3):1–14, 2011.

[24] Y.X. Hou, N.T. Clemens, and D.S. Dolling. Wide-field PIV study of shock-induced turbulent boundary layer separation. *AIAA paper*, 2003-0441, 2003.

[25] R.A. Humble, F. Scarano, and B.W. Van Oudheusden. Particle image velocimetry measurements of a shock wave/turbulent boundary layer interaction. *Experiments in Fluids*, 43(43):173–183, 2007.

[26] P. Krogmann, E. Stanewsky, and P. Thiede. Effects of suction on shock/boundary-layer interaction and shock-induced separation. *Journal of aircraft*, 22(1):37–42, 1985.

[27] S. Lee, E. Loth, and H. Babinsky. Normal shock boundary layer control with various vortex generator geometries. *Computers & Fluids*, 49(1):233–246, 2011.

[28] J.C. Lin. Review of research on low-profile vortex generators to control boundary-layer separation. *Progress in Aerospace Sciences*, 38(4):389–420, 2002.

[29] D.C. McCormick. Shock/boundary-layer interaction control with vortex generators and passive cavity. *AIAA journal*, 31(1):91–96, 1993.

[30] J. Muller, R. Mummler, and W. Staudacher. Comparison of some measurement techniques for shock-induced boundary layer separation. *Aerospace science and technology*, 5(6):383–395, 2001.

[31] H. Ogawa, H. Babinsky, M. Pätzold, and T. Lutz. Shock-wave/boundary-layer interaction control using three-dimensional bumps for transonic wings. *AIAA journal*, 46(6):1442–1452, 2008.

[32] H.H. Pearcey. *Shock-induced separation and its prevention by design and boundary layer control*. Pergamon, 1961.

[33] S. Pirozzoli and F. Grasso. Direct numerical simulation of impinging shock wave/turbulent boundary layer interaction at m= 2.25. *Physics of Fluids*, 18:065113, 2006.

[34] S. Raghunathan and S.T. McIlwain. Further investigations of transonic shock-wave boundary-layer interaction with passive control. *Journal of Aircraft*, 27(1):60–65, 1990.

[35] F. Sartor, G. Losfeld, and R. Bur. PIV study on a shock induced separation in a transonic flow. *Experiments in Fluids*, 53(3):815–827, 2012.

[36] M.S. Selig, J. Andreopoulost, K.C. Muck, J.P. Dussauge, and A.J. Smits. Turbulence structure in a shock wave/turbulent boundary-layer interaction. *AIAA journal*, 27(7):862–869, 1989.

[37] E. Touber and N.D. Sandham. Large-eddy simulation of low-frequency unsteadiness in a turbulent shock-induced separation bubble. *Theoretical and Computational Fluid Dynamics*, 23(2):79–107, 2009.

[38] B.W. van Oudheusden, A.J.P. Jöbsis, F. Scarano, and LJ Souverein. Investigation of the unsteadiness of a shock-reflection interaction with time-resolved particle image velocimetry. *Shock Waves*, 21:1–13, 2011.

[39] S.B. Verma, C. Manisankar, and D. Raju. Control of shock unsteadiness in shock boundary-layer interaction on a compression corner using mechanical vortex generators. *Shock Waves*, 22:327–339, 2012.